

# Supramolecularly Engineered Bulk-Heterojunction Solar Cells with Self-Assembled Non-Fullerene Nanographene Tetraimide Acceptors

Kaan Menekse, Magnus Mahl, Julius Albert, M. A. Niyas, Kazutaka Shoyama, Matthias Stolte,\* and Frank Würthner\*

A series of novel imide-functionalized C<sub>64</sub> nanographenes is investigated as acceptor components in organic solar cells (OSCs) in combination with donor polymer PM6. These electron-poor molecules either prevail as a monomer or self-assemble into dimers in the OSC active layer depending on the chosen imide substituents. This allows for the controlled stacking of electron-poor and electron-rich  $\pi$ -scaffolds to establish a novel class of non-fullerene acceptor materials to tailor the bulk-heterojunction morphology of the OSCs. The best performance is observed for derivatives that are able to self-assemble into dimers, reaching power conversion efficiencies of up to 7.1%.

## 1. Introduction

The bulk-heterojunction (BHJ) concept continues to attract researchers working in organic photovoltaics (OPVs) due to the ongoing advancements in device performance. While the first period in this field was focused on the exploration of composites of already available electron donor polymers such as poly-(3-hexyl)thiophene with fullerenes,<sup>[1,2]</sup> advancement in the second period came from newly designed semiconducting donor polymers with better light harvesting and charge carrier capability.<sup>[3,4]</sup> Current interest in a third period lies in replacing fullerene with non-fullerene acceptors (NFAs), whose contribution to the harvesting of solar light is dramatically improved compared to fullerenes.<sup>[5,6]</sup> However, the morphological stability of many of the currently successful composites is not sufficient, which

relates to the formation of BHJs consisting of thermodynamically unstable domain structures.<sup>[7,8]</sup>


The challenge of designing functional BHJs by stepwise self- and co-assembly of an acceptor (A) and donor (D) component constitutes a long-term goal of our group, as this should allow for a tailored architectures for optimized energy and charge transport.<sup>[9]</sup> Toward this goal, we introduced already in 2004 a supramolecular p-n heterojunction model system<sup>[10]</sup> and in 2010 the concept of self-assembled small molecule donor materials based on

dimer aggregates forming merocyanine dyes.<sup>[11]</sup> In subsequent studies, these afforded solution- and vacuum-processed merocyanine/fullerene BHJ organic solar cells (OSCs) with power conversion efficiencies (PCEs) up to 6.1%.<sup>[12,13]</sup> In contrast, our efforts to self-assemble perylene bisimide (PBI)-based NFAs into suitable functional light-harvesting and charge-transporting supramolecular structures for photocurrent generation in BHJ solar cells remained so far with limited success.<sup>[14,15]</sup> However, pioneering research from the groups of Nuckolls,<sup>[16]</sup> Yan,<sup>[17]</sup> and Wang<sup>[18]</sup> showed that the annulation of multiple PBIs units to either central cores or to oligomers afforded NFAs that yield significantly improved polymer-based OSCs with the best performance (11.2% PCE) currently achieved by a quite sophisticated and challenging to synthesize molecule bearing five PBIs annulated to a corannulene central unit reported by Wang and co-workers in 2021. Accordingly, besides the currently leading acceptor-donor-acceptor (A-D-A) non-fullerene materials,<sup>[19]</sup> imide-functionalized electron-poor polycyclic aromatic hydrocarbons (PAHs) constitute a most promising class of compounds, due to their improved chemical stability.<sup>[20,21]</sup>

In this research article, we investigate a new class of 2D PAHs functionalized with multiple imide units that have been developed recently in our laboratory.<sup>[22,23]</sup> These electron-poor molecules can be considered as 2D analogs of PBIs due to an almost identical lowest unoccupied molecular orbital (LUMO) level, originating from a well-balanced ratio between sp<sup>2</sup>-hybridized carbon atoms in the PAH framework, and the number of electron-withdrawing imide groups (**Figure 1**). However, different from the similarity in electron affinity, a much broader spectral range of visible light is absorbed by the C<sub>64</sub> nanographene tetraimides. Furthermore, the enlarged  $\pi$ -scaffold of these new NFAs offers a better perspective to tailor the intermolecular

K. Menekse, M. Stolte, F. Würthner  
Center for Nanosystems Chemistry (CNC)  
Universität Würzburg  
97074 Würzburg, Germany  
E-mail: matthias.stolte@uni-wuerzburg.de; wuerthner@uni-wuerzburg.de

M. Mahl, J. Albert, M. A. Niyas, K. Shoyama, M. Stolte, F. Würthner  
Institut für Organische Chemie  
Universität Würzburg  
97074 Würzburg, Germany

 The ORCID identification number(s) for the author(s) of this article can be found under <https://doi.org/10.1002/solr.202200895>.

© 2022 The Authors. Solar RRL published by Wiley-VCH GmbH. This is an open access article under the terms of the Creative Commons Attribution License, which permits use, distribution and reproduction in any medium, provided the original work is properly cited.

DOI: 10.1002/solr.202200895

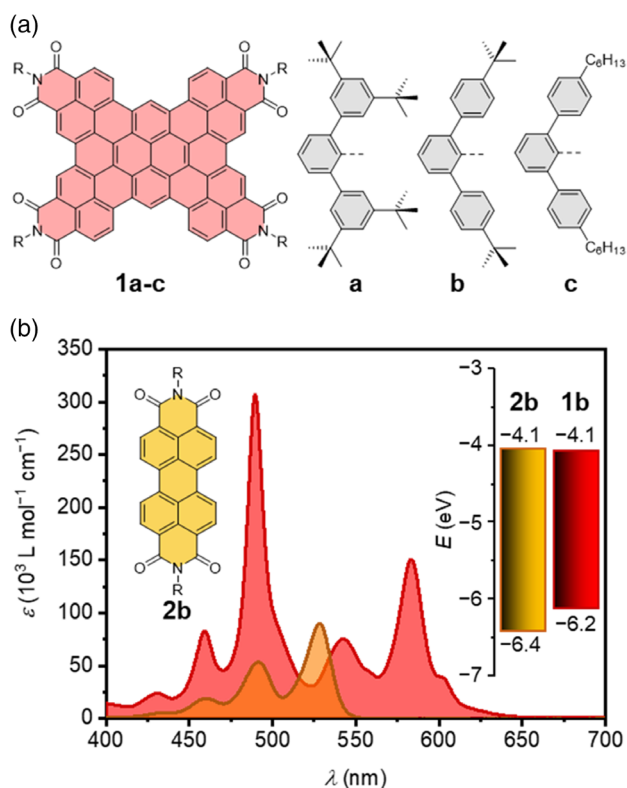


**Figure 1.** a) Molecular structures of here investigated nanographene tetraimides **1a–c** with different 2,6-diphenylphenyl imide substituents (**a–c**) as well as b) a representative UV–vis absorption spectrum of **1b** (red, monomer) in comparison to that of a perylene bisimide **2b** (orange) in CH<sub>2</sub>Cl<sub>2</sub> at 298 K. The inset displays the respective frontier molecular orbitals (HOMOs and LUMOs) and bandgaps (solid area) of **1b**<sup>[24]</sup> (red) and **2b**<sup>[26,29]</sup> (orange) as determined by CV in CH<sub>2</sub>Cl<sub>2</sub> calibrated against the ferrocene/ferrocenium couple (Fc/Fc<sup>+</sup>, –5.15 eV).<sup>[39]</sup> Data extracted from the respective cited references.

interactions of these ditopic host molecules for favorable acceptor–acceptor and acceptor–donor arrangements, which is crucial for the concept of a self-assembled photovoltaic material.

## 2. Results and Discussion

### 2.1. Synthesis and Molecular Properties

Two new C<sub>64</sub> nanographene tetraimides, **1a** and **1c**, as well as their respective precursors, were synthesized according to previously reported procedures by us for compound **1b**.<sup>[24]</sup> Compounds **1a–c** are decorated with imide substituents of different sterical demands, yielding three derivatives with varying solubility as well as self-assembly capability. All imide substituents are based on 2,6-diphenylphenyl moieties with either two *tert*-butyl (*t*Bu) groups in 3,5-positions (**a**), or one *t*Bu (**b**) or *n*-hexyl (**c**) substituent in 4-positions of the outer phenyl groups (Figure 1a). As these eight outer phenyl-residues of all four imide substituents can rotate in solution, the number and positioning as well as the flexibility of their respective alkyl-substituents will control the self-assembly of the C<sub>64</sub> nanographene tetraimides. The synthesis starts

from the respective dibromo naphthalimide precursor, which was then coupled with a tetraboronated pyrene core by a Suzuki cross-coupling reaction and subsequent oxidative dehydrogenation as the final step which yielded the new compounds **1a** and **1c** in 15% and 35%, respectively (Scheme S1, Supporting Information). Larger quantities of all three derivatives were purified by column chromatography as well as HPLC before characterization by <sup>1</sup>H- and <sup>13</sup>C-nuclear magnetic resonance (NMR), UV–vis, and fluorescence spectroscopy as well as high-resolution mass spectrometry (HRMS) and cyclic voltammetry (CV).

UV–vis absorption and fluorescence spectroscopy were initially conducted for diluted samples in dichloromethane (CH<sub>2</sub>Cl<sub>2</sub>) at 298 K. In accordance with our previous reports on C<sub>64</sub> nanographene tetraimides<sup>[24,25]</sup> the broad UV–vis absorption band ( $c_0 = 4 \times 10^{-6} \text{ M}$ ) of **1a–c** is dominated by two prominent absorption maxima ( $\lambda_{\text{max}}$ ) at about 585 and 490 nm, attributable to two orthogonally polarized S<sub>0</sub>–S<sub>1</sub> and S<sub>0</sub>–S<sub>2</sub> transitions. This enables strong absorbance over the full visible range from 400 to 650 nm due to pronounced vibronic progressions (Figure 1b). The molar extinction coefficients ( $\epsilon_{\text{max}}$ ) of these two maxima are in the range of 163 000 (585 nm) and 320 000 M<sup>–1</sup> cm<sup>–1</sup> (490 nm), respectively (Figure S1a, and Table S1, Supporting Information). These large values are promising for application in OPV and outmatch strong absorbing PBIs like **2b**<sup>[26]</sup> with 90 000 M<sup>–1</sup> cm<sup>–1</sup> at 527 nm (Figure 1b). Fluorescence studies of all three derivatives in CH<sub>2</sub>Cl<sub>2</sub> at 298 K ( $c_0 = 10^{-7} \text{ M}$ ) reveal almost mirror image-like emission spectra for the lowest energy S<sub>0</sub>–S<sub>1</sub> transition band with maxima at 604–608 nm and accordingly small Stokes shifts ( $\Delta\tilde{\nu}_{\text{Stokes}}$ ) between 550 and 700 cm<sup>–1</sup> (Figure S2, and Table S1, Supporting Information). In contrast to PBIs<sup>[27,28]</sup> with similar imide substituents (**2b**:  $\Phi_{\text{fl}}$ : 97%,  $\tau$ : 3.8 ns) the herein investigated C<sub>64</sub> nanographene tetraimides show lower fluorescence quantum yields ( $\Phi_{\text{fl}}$ : 62–73%) but significantly longer fluorescence lifetimes ( $\tau$ : 12.0–13.5 ns, Table S1, Supporting Information).

The molecular highest occupied molecular orbital (HOMO) and LUMO levels were experimentally determined by CV for **1a** and **1b**<sup>[24]</sup> in CH<sub>2</sub>Cl<sub>2</sub> ( $c_0 = 2 \times 10^{-5} \text{ M}$ ) with added Bu<sub>4</sub>NPF<sub>6</sub> (0.1 M) and calibrated against the ferrocene/ferrocenium (Fc/Fc<sup>+</sup>) couple. Five reversible reduction potentials were observed and the first reduction potential ( $E_{1/2}^{\text{Red1}}$ ) at  $\approx -1.02$  (**1a**) and  $-1.04 \text{ V}$  (**1b**) of the PAH tetraimides equals the one of unsubstituted PBIs with  $-1.02 \text{ V}$ <sup>[29]</sup> which resemble both LUMO levels at about  $-4.1 \text{ eV}$  with Fc/Fc<sup>+</sup> value of  $-5.15 \text{ eV}$ <sup>[30]</sup> vs. vacuum (Figure 1b, S11, and Table S3, Supporting Information). The first oxidation potential ( $E_{1/2}^{\text{Ox1}}$ ) at  $+1.02 \text{ V}$  leads to an electrochemical bandgap of 2.06 eV, which is well in accordance with the optical bandgap determined from the onset of the tailing short-wavelength absorption band (2.0 eV).

While the molecular optoelectronic properties of all three nanographene tetraimides **1a–c** are almost identical, the impact of their respective imide-substituents on their self-assembly capability was readily apparent during initial studies in CH<sub>2</sub>Cl<sub>2</sub> even at  $c_0 = 4 \times 10^{-6} \text{ M}$ . First indications for a partial association of these nanographenes even in this good solvent for aromatic compounds can be found in the UV–vis absorption spectra of **1b,c** by the more strongly tailing of the red-edged absorption spectra in contrast to **1a** (Figure S1b, Supporting Information). In addition, while all derivatives display a signal for a monomer species [M] in their matrix-assisted laser desorption ionization (MALDI) spectra, for

compounds **1b,c** also a signal of a dimer species [ $M_2$ ] can be clearly observed (Figure S35–S37, Supporting Information). Lastly, these two derivatives also exhibit slightly smaller  $\Phi_f$  (**1b**: 68%, **1c**: 62%) in contrast to the highest value of 73% (**1a**), which could be indicative of the presence of some traces of aggregate species with partially quenched emission (Table S1, Supporting Information). These observations motivated us to have a closer look at the self-assembly capability of this series of nanographene tetraimides in solvent mixtures of lower polarity as well as in solid matrixes.

## 2.2. Aggregation Properties

While  $C_{64}$  nanographene tetraimide dimers were already observed in our previous work in the crystalline state (see also

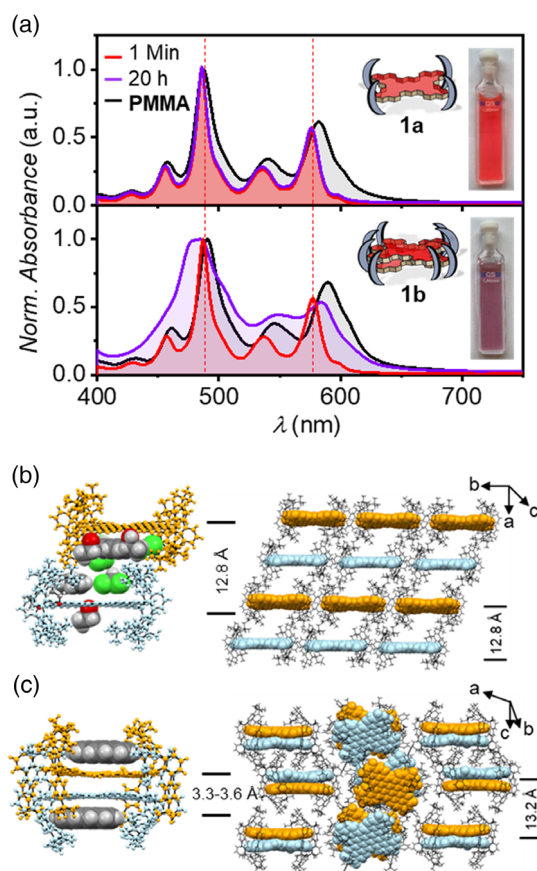


**Figure 2.** a) Normalized UV-vis absorption spectra of nanographene tetraimide **1a** (top) and **1b** (bottom) in a solvent mixture of toluene:methylcyclohexane (1:4,  $c_0 = 5 \times 10^{-6}$  M) measured after 1 min (red) as well as after 1200 min (violet) in comparison to thin film spectra in **PMMA** matrix (black, wt%: 1.0:0.6) spin-cast onto quartz substrates. Insets show aged solutions in THF:methylcyclohexane (2:3,  $c_0 = 10^{-4}$  M) to visualize the color change. Single crystal structures of: b) isolated monomers of **1a** and c) dimers of **1b**<sup>[24]</sup> (in combination with coronene). Illustration of the central molecule and the next neighboring which differ in their planarity (orange, blue) in space-filling, while the imide substituents are displayed in wireframe. Hydrogen atoms, disorder of imide substituents, solvent molecules as well as donor coronene (**1b**<sup>[24]</sup>) are partially omitted for clarity. Data extracted from the respective cited references.

Figure 2c),<sup>[23]</sup> the dimerization process in solution is strongly influenced by kinetic effects and accordingly dependent on the solvent and temperature. Suitable conditions to monitor the aggregation via time-dependent UV-vis absorption measurement were found with mixtures of toluene:methylcyclohexane at 298 K ( $c_0 = 10^{-6}$  M). For the most shielded compound, **1a**, no significant spectral changes are observable over the extended time period of 20 h. However, the derivatives **1b** and **1c** with their more accessible  $\pi$ -surfaces display distinct changes (Figure 2a, S3–S5, Supporting Information). For **1b**, the absorption spectra broaden, decrease in intensity, and show bathochromic as well as hypsochromic shifts of their two main absorption maxima at 577 and 488 to 583 and 484 nm, respectively (Figure 2a). Multiple isosbestic points at 587, 561, 548, 523, 504, 479, 462, 447, 443, and 420 nm can be observed during the self-assembly of **1b** which indicate the existence of an equilibrium between the monomer and a defined aggregate, presumably a dimer species (vide infra). For **1b**, this process is clean and attributable to a kinetic self-assembly process that can be followed over a time course of 20 h. For **1c**, the process is faster but cannot be followed to the very end due to the formation of precipitates (Figure S4, Supporting Information). It is noteworthy that the self-assembled aggregates of **1b** remain stable upon heating the sample solution up to 353 K and show no evidence of disassembly.

To further elaborate on these findings for the production of the active layer morphology with donor polymer **PM6**, we embedded each nanographene tetraimide **1a–c** in a poly(methyl methacrylate) (**PMMA**) matrix (Figure S6, S7, and Table S2, Supporting Information) to simulate their self-assembly in the BHJ.<sup>[31]</sup> As for the OPV devices, we used a D:A blend solution (1.0:0.6; with D: **PMMA**) with a total concentration of 12 mg mL<sup>-1</sup> in chlorobenzene for thin-film deposition, which was spin-cast at 750 rpm for 60 s onto quartz substrates without the addition of any additives. The recorded UV-vis absorption spectra of the nanographenes in the **PMMA** matrix match well with the obtained shapes of the active layer after subtraction of the spectral **PM6** contribution to the total absorption of the BHJ (Figure S8–S10, Supporting Information).

The self-assembly of **1b** and **1c** into aggregates within the **PMMA** matrix can be observed by similar changes in the UV-vis absorption spectra as during aggregation over time in the low-polarity solvent mixture (Figure S4, Supporting Information). In contrast, the most-shielded **1a** retains a similar spectral shape to the monomers in solution with only a slight red-shift due to polarization effects by the matrix. This indicates a homogeneous dispersion of the monomeric nanographenes in the solid polymer matrix (Figure 2a). Likewise for the fluorescence spectra, where the embedded monomers of **1a** exhibit the least bathochromically shifted and most structured emission spectrum ( $\lambda_{em} = 681$  nm), while the  $\pi$ -stacked aggregates of **1b** and **1c** in **PMMA** displayed broad structureless fluorescence spectra with  $\lambda_{em}$  at 716 and 753 nm, respectively, resembling excimer-like emission spectra of PBI H-aggregates.<sup>[32]</sup> Of course, one has also to take reabsorption as well as Förster resonance energy transfers (FRET) from the monomer to aggregates, as it was described by Zhang et al. for PBIs,<sup>[33]</sup> for these high-concentrated solids into account. Still, **1a** behaves clearly differently to **1b,c**, which must be related to its sterically most-shielding imide substituents, which render the

nanographene  $\pi$ -surface inaccessible for  $\pi$ - $\pi$ -stacking interactions with other nanographene **1a** molecules.

Additional support for the dimer formation is provided by comparing the single crystal X-ray structures of derivatives **1a** and **1b**<sup>[24]</sup> (Figure 2b,c, S12 and S13, and Table S4 (CCDC2205851), Supporting Information). Unfortunately, we were not able to obtain suitable single crystal for X-ray crystallography of derivative **1c** that contains the flexible hexyl-substituents. While the crystal structures of **1a** and **1b** contain solvent and guest molecules (**1b**:coronene) that occupy the crystal voids originating from the sterically demanding imide-substituents, a clear difference in molecular stacking and interaction of these two C<sub>64</sub> nanographene tetraimides was observed. The single crystal of **1a** showed no tendency for any  $\pi$ - $\pi$  stacking, and thus the molecules arrange as isolated monomers with only minor edge-to-edge contacts towards four in-plane neighboring molecules (Figure 2b). These 2D layers of parallelly oriented nanographene  $\pi$ -surfaces are separated from each other by about 12.8 Å. In comparison, **1b** tends to form defined  $\pi$ -stacked dimeric assemblies (3.2–3.4 Å) and are each topped by a guest molecule in the solid state (3.3–3.6 Å), which are separated from each other at distances of 13.2 Å (Figure 2c).<sup>[24]</sup> These stacked dimers should exhibit H-type coupling in accordance with the earlier discussed spectral changes in low polar solvent mixtures as well as PMMA matrix (Figure S4–S7, Supporting Information). We, therefore, infer that within the BHJ, the two remaining  $\pi$ -surfaces of the ditopic electron-poor C<sub>64</sub> nanographene tetraimide dimer, now each occupied by coronene molecule, are easily accessible to electron-rich  $\pi$ -scaffolds of the donor polymer by either  $\pi$ - $\pi$  or CH- $\pi$  interactions. In addition, the steric crowding imparted by bulky imide substituents around the C<sub>64</sub> nanographene dimer indicates that the formation of larger extended aggregates than a dimer for **1b,c**, which could lead to demixing of the blend, is unfavored.

The preferential preorganization of **1b** and **1c** into discrete dimers with two accessible  $\pi$ -surfaces is assumed to occur during the spin-coating process used to form the BHJ with **PM6** given that the UV-vis absorption spectra are similar (Figure S8–S10, Supporting Information). In contrast, the most-shielded derivative **1a** is incorporated into the polymer matrix as monomeric species with only limited  $\pi$ -contact to **PM6**.

### 2.3. Polymer-Based OSCs

The impact of the different preorganization on the OPV performance within this series of electron acceptor materials (**1a–c**) was investigated in combination with the high-performance donor polymer **PM6** in an inverted ITO/ZnO(20 nm)/**PM6:1a–c** (90 nm)/MoO<sub>3</sub>(10 nm)/Al(100 nm) device architecture (Figure 3a). This D–A material combination exhibits good spectral coverage of sunlight up to 700 nm as well as an appropriate HOMO(D)–LUMO(A) gap for efficient charge separation at their interface in the BHJ (Figure S15, Supporting Information). All BHJ active layers of the OSCs were applied onto ZnO-coated glass/ITO substrates by spin-coating (750 rpm, 60 s) a chlorobenzene solution at a total concentration of 12 mg mL<sup>-1</sup> with a weight ratio of 1.0:0.6 (D:A). To support the self-assembly of our NFAs

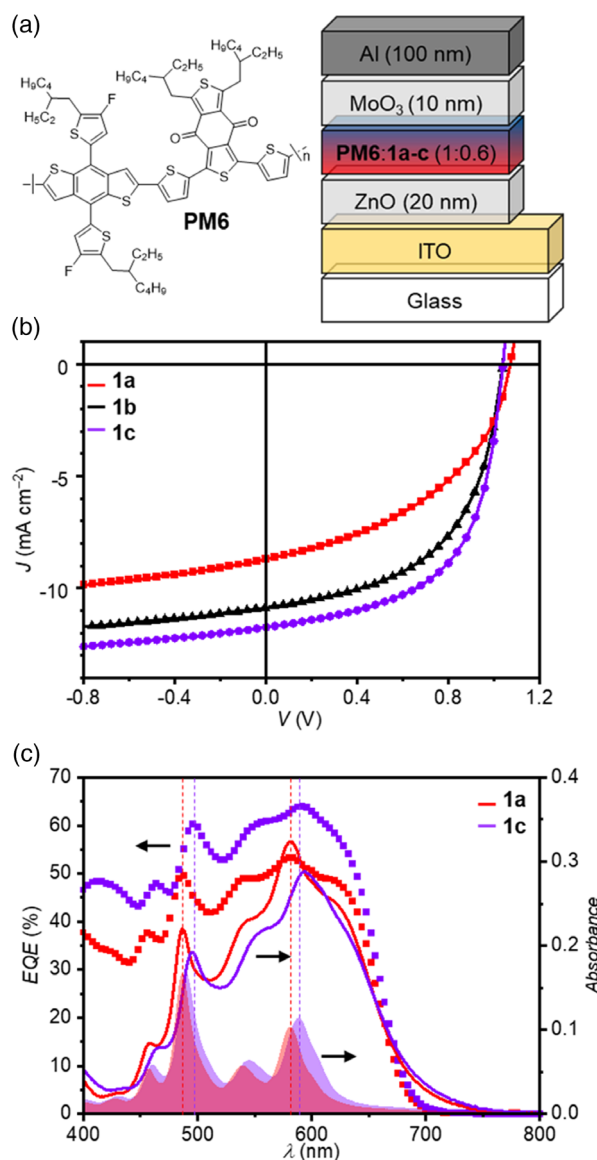


**Figure 3.** a) Chemical structure of donor polymer **PM6** used in excess of 1:0:0.6 (wt%) with the nanographene tetraimides **1a–c** as well as the schematic representation of the architecture of the solution-processed inverted BHJ OSCs in ITO/ZnO/**PM6:1a–c**/MoO<sub>3</sub>/Al architecture. b) Representative *J*-*V* curves of shielded NFAs **1a** (red), **1b** (black), and **1c** (purple) containing OSCs in combination with **PM6** as donor material, which were measured under inert conditions and AM1.5 G irradiation. c) Representative external quantum efficiency (EQE, symbols) and UV-vis absorption (solid line) spectra of the BHJ OSCs based on derivatives **1a** (red) and **1c** (purple). For the assignment of the contribution of the acceptor species to the photocurrent, the absorption spectra of thin films of **1a** (red) and **1c** (purple) in the **PMMA** matrix (shaded area) as well as vertical dashed lines for the most important absorption maxima thereof are displayed as well.

(Figure S3–S5, Supporting Information) we stirred each blend solution for at least 3 h at 298 K after the combination of the respective D and A solutions. The mixing ratio 1.0:0.6 yielded the highest power conversion efficiencies (PCEs) and afforded equal layer thicknesses of approximately 90 nm for all three NFAs. Higher



content of C<sub>64</sub> nanographene tetraimides as well as solvent additives or any annealing (thermal/solvent) had no positive effects on the optimized performances obtained under AM 1.5 G illumination.

The main figure of merit for an OPV device is the PCE, which is calculated by the product of the photocurrent density generated by the device under short-circuit conditions ( $J_{SC}$ ), the voltage under open-circuit conditions ( $V_{OC}$ ), and the fill factor (FF) divided by the incident light power ( $P_{Light}$ ). While all OSCs of the new nanographene tetraimides show appropriate diode-like behavior under AM 1.5 G light illumination in combination with donor polymer **PM6**, their PCEs show pronounced differences. Representative  $J$ - $V$  curves of all OSCs are shown in Figure 3b (dark curves: Figure S17, Supporting Information), while their characteristic OPV parameters are listed in Table 1. At first glance, the observed diode-like behavior is surprising considering that the rigid bulky imide substituents prohibit close contacts between the respective  $\pi$ -surfaces of neighboring nanographene monomers or dimers, respectively, which are prerequisites to enable efficient percolation pathways for charge-transport (Figure 2b,c).

Devices containing the most-shielded derivative **1a**, which prevails mainly monomeric in the BHJ, yielded a peak efficiency (PCE<sub>max</sub>) of up to 4.2%, due to its lower  $J_{SC}$  and FF in comparison to the other derivatives. The dimer-forming NFA **1b** afforded performances up to 6.4%, while **1c** with its higher solubility led to the highest PCE<sub>max</sub> of up to 7.1%. To gain a deeper understanding of these appreciably high efficiencies, a detailed analysis of the respective devices as well as their active layers needs to be conducted.

As all of the nanographene tetraimides investigated here possess their  $E_{1/2}^{Red1}$  at about  $-1$  V (Table S3, Supporting Information) in solution, they should also show similar  $V_{OC}$ . These are indeed almost equal and relatively high with values ranging from 1.04 V for **1b** and **1c** up to even 1.08 V for **1a** (Figure 3b, Table 1). We assume, that the  $V_{OC}$  value is directly related to the respective molecular arrangement in the NFA domains, rather than to interface effects within the devices. Investigations of the morphology of all blends by atomic force microscopy (AFM) did not reveal distinguishable separated donor or acceptor domains which could be related to effects at the interfaces to interlayers and/or electrodes (Figure S14 and S15, Supporting Information). All active layers exhibit very similar and smooth surfaces with an average roughness of about 1.66 nm (**1a**), 1.27 nm (**1b**), and 1.24 nm (**1c**) at a  $5 \times 5$  mm<sup>2</sup> surface area. This provides further evidence for very homogenous

and well-mixed BHJs with presumably only nanometer-scaled acceptor domains, which appear according to the AFM phase images for the monomeric derivative **1a** (<6 nm) to be smaller than for the dimer-containing nanographenes **1b** (<15 nm) and **1c** (<15 nm) (Figure S15, Supporting Information).

Interestingly, the OSCs containing the NFAs **1a–c** exhibit high but different  $J_{SC}$  values of  $-8.59$  (**1a**),  $-10.75$  (**1b**), and  $-10.79$  (**1c**) mA cm<sup>-2</sup>, respectively (Figure 3b, Table 1), while their individual active layer's absorbance and consequent light harvesting capability are almost equal (Figure 3c, and S6, Supporting Information). Based on this data, it would suggest that the edge-to-edge connected monomers, as in the case of **1a**, show a significantly higher recombination rate than the preassembled dimers in the case of **1b** and **1c**. Investigations by light-power-dependent  $J$ - $V$  measurements of all OPV devices confirmed that the dimer-containing BHJ of **1c** has the best donor-acceptor interface as well as a lower trap density with respect to the BHJs based on combinations with **1a** and **1b** (Figure S19, and Table S5, Supporting Information). Therefore, a closer inspection of the respective external quantum efficiency (EQE) spectra in combination with the UV-vis absorption spectra of the active layers are needed (Figure 3c, and S18, Supporting Information). In general, the short-circuit current density determined by the integration of the EQE ( $J_{sc}^{EQE}$ ) equals quite well the values of  $J_{SC}$  determined by the  $J$ - $V$  curves (Table 1). Here, small similar changes in the EQE and in the absorption maxima for **1b** and **1c**, like a decrease in intensity as well as a shift of characteristic maxima, can again be traced back to the formation of dimers (**1b,c**) and to their contribution to the photocurrent (Figure 2a). This, however, seems to be more efficient in domains of self-assembled dimers (**1b,c**), as for monomers (**1a**) dispersed in **PM6**. The contribution of the nanographene tetraimides to the overall photocurrent generation can be clearly distinguished, reaching EQE values as high as 64% at 591 nm for the dimeric **1b,c**, while **1a** as monomers only achieve 53% at 580 nm (Figure 3c).

The third parameter to be discussed is FF, which gives some information about the balance between electron and hole mobilities as well as recombination pathways in the respective OSCs. These values range from 44% for **1a**, over 54% for **1b**, and up to 57% for **1c** (Table 1). This indicates that the formation of closely stacked dimers in combination with a higher solubility of **1c** is facilitating an improved electron transport in the NFA domains if the hole transport in **PM6** stays equal. To verify these insights into the charge-transport properties of the active layers, SCLC devices were processed in ITO/PEDOT:PSS/BHJ/MoO<sub>3</sub>/Al

**Table 1.** Summary of the photovoltaic parameters of optimized inverted BHJ OSCs in ITO/ZnO/**PM6:1a–c** (1.0:0.6)/MoO<sub>3</sub>/Al architecture measured under inert conditions and under AM 1.5 G irradiation. Charge carrier mobilities ( $\mu_h/\mu_e$ ) were determined by space-charge-limited current (SCLC) devices processed in ITO/PEDOT:PSS/BHJ/MoO<sub>3</sub>/Al (hole-only device; HOD) and in ITO/ZnO/BHJ/PDINO/Al (electron-only device, EOD) architectures with the same active layer as in the OSC experiments.

NFA	$J_{SC}^{a)}$ [mA cm <sup>-2</sup> ]	$J_{sc}^{EQE}$ [mA cm <sup>-2</sup> ]	$V_{OC}^{a)}$ [V]	FF <sup>a)</sup> [%]	PCE <sup>a)</sup> [%]	PCE <sub>max</sub> [%]	$\mu_h$ [cm <sup>2</sup> V <sup>-1</sup> s <sup>-1</sup> ]	$\mu_e$ [cm <sup>2</sup> V <sup>-1</sup> s <sup>-1</sup> ]
<b>1a</b>	$-8.6 \pm 0.2$	$-7.7$	$1.08 \pm 0.01$	$44 \pm 1$	$4.1 \pm 0.1$	4.2	$10 \times 10^{-4}$	$0.5 \times 10^{-7}$
<b>1b</b>	$-10.7 \pm 0.5$	$-9.6$	$1.02 \pm 0.02$	$54 \pm 1$	$6.0 \pm 0.2$	6.4	$5 \times 10^{-4}$	$1.0 \times 10^{-7}$
<b>1c</b>	$-10.8 \pm 0.5$	$-9.7$	$1.04 \pm 0.01$	$56 \pm 1$	$6.3 \pm 0.5$	7.1	$10 \times 10^{-4}$	$50 \times 10^{-7}$

<sup>a)</sup>Average of at least 15 independent devices.

(hole-only device; HOD) and in ITO/ZnO/BHJ/PDINO/Al (EOD) architectures with the same active BHJ layer as in the OSC experiments (for details see Figure S20 and S21, Supporting Information). While the hole mobility ( $\mu_h$ ), which is connected to the donor polymer **PM6**, is overall high and of equal magnitude in the range of  $5\text{--}10 \times 10^{-4} \text{ cm}^2 \text{ V}^{-1} \text{ s}^{-1}$ , the electron mobility ( $\mu_e$ ) differs significantly for the respective NFAs (Table 1). While **1a** exhibits the lowest mobility in the range of  $10^{-8} \text{ cm}^2 \text{ V}^{-1} \text{ s}^{-1}$ , higher values of up to  $10^{-6} \text{ cm}^2 \text{ V}^{-1} \text{ s}^{-1}$  were observed for **1b** and **1c**, enabling a more balanced charge transport in the active layer. Therefore, it can be concluded that the 2,6-bis(4-hexylphenyl)phenyl imide substituents of **1c** are the most potent nanographene modification combining the best film-forming ability as well as a dimer-containing packing arrangement for optimal charge-transport followed by the *tert*-butylphenyl (**1b**) and the di-*tert*-butylphenyl (**1a**) substituted derivatives. This demonstrates the favorable effect of the supramolecularly engineered  $\pi$ -stacked dimers in the NFA domains, which still retain accessible  $\pi$ -surfaces for interactions with the donor polymer **PM6**, to realize a PCE<sub>max</sub> of up to 7.1% for C<sub>64</sub> nanographene tetraimide **1c**.

### 3. Conclusion

Here, a series of three C<sub>64</sub> nanographene tetraimides bearing different sterically demanding imide modifications based on 2,6-diphenylphenyl substituents have been studied for the first time as acceptor components in polymer solar cells. We studied their different self-assembly behavior by UV-vis absorption and emission measurements in solution as well as in the **PMMA** matrix. In combination with their respective single-crystal X-ray structures, we linked these observations to the archived

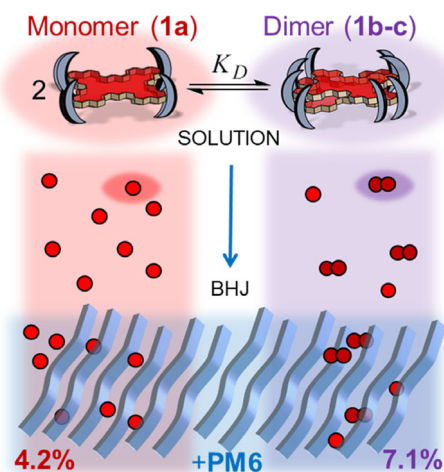


**Figure 4.** Concept for the stepwise self-assembled materials in the BHJ morphology realized in this work. Pending the accessibility of the electron-poor nanographene tetraimides'  $\pi$ -surfaces, the molecules self-assemble in solution partially into dimers (**1b,c**) or remain as monomers (**1a**). The subsequent formulation and processing with donor polymer **PM6** results in homogeneously mixed active BHJ layers, where either these species remain isolated (left: **1a**) or dimerized (right: **1b-c**) and being embedded in a matrix of electron-rich polymer sections.

solar cell performances. The derivative **1a** with the most-shielding imide-substituent, which consists of two *t*Bu groups in the 3,5-position, strongly disfavors aggregation, leading to a monomeric dispersion of nanographenes in the donor polymer matrix of the solar cell affording a maximum PCE of only 4.2% in combination with **PM6** (Figure 4). A decoration of one *t*Bu in the 4-position already leads to the preorganization into  $\pi$ -stacked dimers in solution, yielding an efficiency of up to 6.4% of the BHJ (Figure 4). Further optimization of the imide substituent was performed by introducing an *n*-hexyl in the 4-position, which still favors the self-assembly into dimers but additionally enables an enhanced solubility with close  $\pi$ -contact toward the donor polymer enabling a peak PCE of up to 7.1% (Figure 4). Our work demonstrates that this remarkable class of new NFAs does not need the formation of extended  $\pi$ -stacked networks, which can be traced back to the large  $\pi$ -surface, still facilitating sufficient electron transport and offering donor-acceptor interactions. Ongoing studies will elucidate if the further enlargement of the  $\pi$ -surface can increase the electron mobility while additionally expanding the absorbance up to the near-infrared region.

### 4. Experimental Section

**Synthesis:** The synthetic procedure for NFA **1b**<sup>[24]</sup> was already reported by the authors, for the procedures for the new materials **1a** and **1c** as well as their characterization, see the Supporting Information.

**UV-vis Absorption Spectroscopy:** UV-vis absorption spectroscopy in CH<sub>2</sub>Cl<sub>2</sub> was measured at room temperature on a Jasco V770 spectrophotometer in 10 mm cuvettes (SUPRASIL, Hellma Analytics). For the thin-film spectra on quartz substrates (SUPRASIL, Hellma Analytics) as well as of the active layer of the OSCs, a Perkin Elmer Lambda 950 spectrometer with an integration sphere was used. The **PMMA**-based thin films of the investigated compounds were fabricated by spin coating a blend of poly(methyl methacrylate) (**PMMA**; Sigma Aldrich,  $M_w \approx 120\,000$ ) and the respective NFA on quartz substrates (1.0:0.6,  $c_{\text{Total}} = 12 \text{ mg mL}^{-1}$  in CB, 750 rpm, 60 s).

**Fluorescence Spectroscopy:** Fluorescence spectroscopy in CH<sub>2</sub>Cl<sub>2</sub> solution ( $10^{-6} \text{ M}$ ,  $A_{\text{max}} < 0.2$ , spectroscopic grade, Uvasol, Merck) as well as in the thin film were measured at room temperature on an Edinburgh Instruments FLS980-D2D2-ST spectrometer and were corrected against the photomultiplier sensitivity and the lamp intensity. Fluorescence lifetimes were determined with an EPL picosecond pulsed diode laser ( $\lambda_{\text{Ex}} = 505.8 \text{ nm}$ ) for time-correlated single-photon counting (TCSPC) with the same spectrometer. Fluorescence quantum yields were measured in CH<sub>2</sub>Cl<sub>2</sub> on a Hamamatsu Absolute PL Quantum Yield Measurement System CC9920-02.

**NMR-Spectroscopy:** NMR-Spectroscopy was performed on a Bruker Avance III HD 400 MHz NMR spectrometer relative to residue undeuterated solvent signals. The chemical shifts ( $\delta$ ) were listed in parts per million (ppm). Multiplicities for proton signals are abbreviated as s, d, t, and m for singlet, doublet, triplet, and multiplet, respectively.

**Mass Spectrometry:** Mass spectrometry was performed in the negative mode via MALDI-TOF on a Bruker Daltonics UltrafleXtreme with 2-[(2*E*)-3-(4-*tert*-butylphenyl)-2-methylprop-2-enylidene] malononitrile (DCBT) as a matrix or via ESI on a Bruker Daltonics microTOF focus.

**Cyclic and Differential Pulse Voltammetry:** Cyclic and differential pulse voltammetry was performed using a measurement setup from Bas Epsilon. A Pt disc electrode and a Pt wire electrode were used as working and counter electrode, respectively, while an AgCl/Ag electrode acted as a reference electrode. The measurement was conducted by adding tetrabutylammonium hexafluorophosphate (0.1 M) in CH<sub>2</sub>Cl<sub>2</sub> with ferrocene as the internal standard.

**Single Crystal Structure:** Single crystal X-Ray diffraction for compound **1a** was measured at  $100 \pm 1 \text{ K}$  on a Bruker D8 Quest Kappa diffractometer

with a Photon II CMOS detector and multilayered mirror with monochromated  $\text{CuK}_\alpha$  radiation. The structure was solved by SHELXT,<sup>[34]</sup> and expanded with Fourier techniques, and refined by SHELXL software package.<sup>[35]</sup>

OSCs: OSCs were processed on ITO-glass substrates (Soluxx GmbH), which were cleaned by sonication with acetone, detergent solution (mucosol), deionized water, and isopropanol, followed by a UV/ozone treatment for 30 min. Afterward, the ZnO layer was applied by spin coating a colloidal solution of ZnO (according to Sun et al.<sup>[36]</sup>) and annealed for 1 h at 200 °C. The ITO/ZnO substrates were transferred to a nitrogen-filled glovebox (M. Braun Inertgas Systeme GmbH;  $c(\text{O}_2) < 0.1$  ppm,  $c(\text{H}_2\text{O}) < 0.1$  ppm), where the active layers were deposited via spin coating. Therefore, the blend solutions were prepared at room temperature by dissolving the respective NFA molecule in chlorobenzene (CB, 4.5 mg mL<sup>-1</sup>; 3 h). The acceptor was mixed (1.0:0.6) with the donor polymer **PM6** (7.5 mg mL<sup>-1</sup>, Brilliant Matters Inc) and stirred overnight. Spin coating was performed at 750 rpm for 60 s. To complete the solar cells,  $\text{MoO}_3$  ( $d = 10$  nm,  $r = 0.2 \text{ \AA s}^{-1}$ ,  $\omega_{\text{rot}} = 10$  rpm,  $p < 10^{-6}$  mbar) was deposited as a hole-transporting layer and aluminum ( $d = 100$  nm,  $r = 2-3 \text{ \AA s}^{-1}$ ,  $\omega_{\text{rot}} = 0$  rpm,  $p < 10^{-6}$  mbar) as electrode material using the OPTIvap-XL from CreaPhys GmbH. The resulting solar cells were measured as cast and under inert conditions.  $J-V$  measurements were performed after calibration with a standard silicon solar cell with a KG filter (ISE Freiburg) under an AM1.5 G Oriol Sol3ATM Class AAA solar simulator (Newport) by a parameter analyzer (Botest Systems GmbH). EQE measurements were carried out with a Quantum Efficiency/IPCE Measurement Kit (Newport) by using a 300 W Xe lamp and a Cornerstone monochromator with an SR810 Lock-In Amplifier for detection. Hole-only and electron-only devices for calculating the SCLC mobility were fabricated with the same procedure for the active layer as for the OSC manufacture. While the hole-only devices (HOD) structures consist of ITO/PEDOT:PSS/BHJ/ $\text{MoO}_3$ /Al the electron-only devices (EOD) were fabricated in ITO/ZnO/BHJ/PDINO/Al architecture. PEDOT:PSS (Heraeus, Clevios O VO Ak 4083) were deposited onto ITO substrates (2500 rpm, 60 s) followed by an annealing step at 150 °C for 15 min. PDINO was synthesized according to Zhang et al.<sup>[37]</sup> and solubilized in methanol (1 mg mL<sup>-1</sup>) and deposited onto the BHJ layer (3000 rpm, 60 s). The calculation of the respective mobilities was performed analogous to Zhu et al.<sup>[38]</sup> The remaining layers ( $\text{MoO}_3$ , ZnO, Al) were fabricated according to the OSC manufacture. The  $J-V$  characteristics of the HOD- and EOD-devices were measured using an Agilent 4055C parameter analyzer on a Cascade EPS150 probe station.

AFM Morphologies of thin films were investigated with NT-MDT Next Solver System in semi-contact mode using a SCOUT 350 RAI (Nu Nano Ltd) silicon cantilevers with a resonance frequency of  $\approx 350$  kHz and a spring constant of  $\approx 42$  N m<sup>-1</sup>. High-resolution AFM images were recorded under ambient conditions using a Bruker Multimode 8 SPM system operating in the tapping mode in air. Silicon cantilevers (OMCL-AC240TS, Olympus) with a resonance frequency of  $\approx 70$  kHz and a spring constant of  $\approx 1.7$  N m<sup>-1</sup> were used.<sup>[34-39]</sup>

CCDC 2205 851 contains the supplementary crystallographic data for this article. These data can be obtained free of charge from The Cambridge Crystallographic Data Centre via [www.ccdc.cam.ac.uk/data\\_request/cif](http://www.ccdc.cam.ac.uk/data_request/cif).

## Supporting Information

Supporting Information is available from the Wiley Online Library or from the author.

## Acknowledgements

The authors thank the Bavarian Ministry for Science and the Arts (Research Program "Solar Technologies Go Hybrid") and the German Research Foundation (DFG, grant Wu317/20-2) for the financial support.

Open Access funding enabled and organized by Projekt DEAL.

## Conflict of Interest

The authors declare no conflict of interest.

## Data Availability Statement

The data that support the findings of this study are available from the corresponding author upon reasonable request.

## Keywords

nanographene, non-fullerene acceptors, organic solar cells, polycyclic aromatic hydrocarbons, self-assembly

Received: October 7, 2022

Revised: November 11, 2022

Published online: December 7, 2022

- [1] F. Padinger, R. S. Rittberger, N. S. Sariciftci, *Adv. Funct. Mater.* **2003**, *13*, 85.
- [2] Y. Kim, S. A. Choulis, J. Nelson, D. D. C. Bradley, S. Cook, J. R. Durrant, *Appl. Phys. Lett.* **2005**, *86*, 063502.
- [3] H. J. Son, F. He, B. Carsten, L. Yu, *J. Mater. Chem.* **2011**, *21*, 18934.
- [4] Z. Zheng, H. Yao, L. Ye, Y. Xu, S. Zhang, J. Hou, *Mater. Today*, **2020**, *35*, 115.
- [5] C. Yan, S. Barlow, Z. Wang, H. Yan, A. K.-Y. Jen, S. R. Marder, X. Zhan, *Nat. Rev. Mater.* **2018**, *3*, 18003.
- [6] A. Armin, W. Li, O. J. Sandberg, Z. Xiao, L. Ding, J. Nelson, D. Neher, K. Vandewal, S. Shoaee, T. Wang, H. Ade, T. Heumüller, C. Brabec, P. Meredith, *Adv. Energy Mater.* **2021**, *11*, 20003570.
- [7] J. H. Kim, T. Schembri, D. Bialas, M. Stolte, F. Würthner, *Adv. Mater.* **2022**, *34*, 2104678.
- [8] A. Venkateswararao, K.-T. Wong, *Bull. Chem. Soc. Jpn.* **2021**, *94*, 812.
- [9] C. J. Schaffer, C. M. Palumbiny, M. A. Niedermeier, C. Jendrzewski, G. Santoro, S. V. Roth, P. Müller-Buschbaum, *Adv. Mater.* **2013**, *25*, 6760.
- [10] M. Ghasemi, H. Hu, Z. Peng, J. J. Rech, I. Angunawela, J. H. Carpenter, S. J. Stuard, A. Wadsworth, I. McCulloch, W. You, H. Ade, *Joule* **2019**, *3*, 1328.
- [11] A. Levitsky, S. A. Schneider, E. Rabkin, M. I. F. Toney, G. L. Frey, *Mater. Horiz.* **2021**, *8*, 1272.
- [12] S. Guo, Y. Hu, M. Qin, J. Li, Y. Wang, J. Qin, P. Cheng, *Mater. Horiz.* **2022**, *9*, 2097.
- [13] C. Caddeo, J. Ackermann, A. Mattoni, *Sol. RRL* **2022**, *6*, 2200172.
- [14] X. Yuan, Y. Zhao, T. Zhan, J. Oh, J. Zhou, J. Li, X. Wang, Z. Wang, S. Pang, P. Cai, C. Yang, Z. He, Z. Xie, C. Duan, F. Huang, Y. Cao, *Energy Environ. Sci.* **2021**, *14*, 5530.
- [15] K.-T. Wong, D. M. Bassani, *NPG Asia Mater.* **2014**, *6*, 116.
- [16] F. Würthner, Z. Chen, F. J. M. Hoeben, P. Osswald, C.-C. You, P. Jonkheijm, J. V. Herrikhuyzen, A. P. H. J. Schenning, P. P. A. M. van der Schoot, E. W. Meijer, E. H. A. Beckers, S. C. J. Meskers, R. A. J. Janssen, *J. Am. Chem. Soc.* **2004**, *126*, 10611.
- [17] F. Würthner, K. Meerholz, *Chem. Eur. J.* **2010**, *16*, 9366.
- [18] V. Steinmann, N. M. Kronenberg, M. R. Lenze, S. M. Graf, D. Hertel, K. Meerholz, H. Bürckstümmer, E. V. Tulyakova, F. Würthner, *Adv. Energy Mater.* **2011**, *1*, 888.
- [19] A. Arjona-Esteban, J. Krumrain, A. Liess, M. Stolte, L. Huang, D. Schmidt, V. Stepanenko, M. Gsänger, D. Hertel, K. Meerholz, F. Würthner, *J. Am. Chem. Soc.* **2015**, *137*, 13524.

- [20] B. Mahlmeister, R. Renner, O. Anhalt, M. Stolte, F. Würthner, *J. Mater. Chem. C* **2022**, *10*, 2581.
- [21] M. Hecht, T. Schlossarek, M. Stolte, M. Lehmann, F. Würthner, *Angew. Chem. Int. Ed.* **2019**, *58*, 12979.
- [22] M. Ball, B. Zhang, B. Fowler, S. Xiao, F. Ng, M. Steigerwald, C. Nuckolls, *Acc. Chem. Res.* **2019**, *52*, 1068.
- [23] Y. Duan, X. Xu, H. Yan, W. Wu, F. Li, Q. Peng, *Adv. Mater.* **2017**, *29*, 1605115.
- [24] M. Mahl, M. A. Niyas, K. Shoyama, F. Würthner, *Nat. Chem.* **2022**, *14*, 457.
- [25] S. Seifert, K. Shoyama, D. Schmidt, F. Würthner, *Angew. Chem. Int. Ed.* **2016**, *55*, 6390.
- [26] M. Mahl, K. Shoyama, A.-M. Krause, D. Schmidt, F. Würthner, *Angew. Chem. Int. Ed.* **2020**, *59*, 13401.
- [27] S. Chen, D. Meng, J. Huang, M. Liang, Y. Li, F. Liu, H. Yan, Z. Wang, *CCS Chem.* **2021**, *3*, 78.
- [28] D. Li, X. Zhang, D. Liu, T. Wang, *J. Mater. Chem. A* **2020**, *8*, 15607.
- [29] A. Nowak-Król, K. Shoyama, M. Stolte, F. Würthner, *Chem. Commun.* **2018**, *98*, 13763.
- [30] W. Jiang, Z. Wang, *J. Am. Chem. Soc.* **2022**, *144*, 14976.
- [31] Y. Wu, S. Schneider, Y. Yuan, R. M. Young, T. Francese, I. F. Mansoor, P. J. Dudas, Y. Lei, E. D. Gomez, D. M. DeLongchamp, M. C. Lipke, G. Galli, M. R. Wasielewski, J. B. Asbury, M. F. Toney, Z. Bao, *Adv. Mater.* **2022**, *12*, 2103957.
- [32] C. Kaufmann, D. Bialas, M. Stolte, F. Würthner, *J. Am. Chem. Soc.* **2018**, *140*, 9986.
- [33] B. Zhang, H. Soleimaninejad, D. J. Jones, J. M. White, K. P. Ghiggino, T. A. Smith, W. W. H. Wong, *Chem. Mater.* **2017**, *29*, 8395.
- [34] G. M. Sheldrick, *Acta Crystallogr. A* **2015**, *71*, 3.
- [35] G. M. Sheldrick, *Acta Crystallogr. C* **2015**, *71*, 3.
- [36] Y. Sun, J. H. Seo, C. J. Takacs, J. Seifert, A. J. Heeger, *Adv. Mater.* **2011**, *23*, 1679.
- [37] Z.-G. Zhang, B. Qi, Z. Jin, D. Chi, Z. Qi, Y. Li, J. Wang, *Energy Environ. Sci.* **2014**, *7*, 1966.
- [38] W. Zhu, J. M. Alzola, T. J. Aldrich, K. L. Kohlstedt, D. Zheng, P. E. Hartnett, N. D. Eastham, W. Huang, G. Wang, R. M. Young, G. C. Schatz, M. R. Wasielewski, A. Facchetti, F. S. Melkonyan, T. J. Marks, *ACS Energy Lett.* **2019**, *4*, 2695.
- [39] C. M. Cardona, W. Li, A. E. Kaifer, D. Stockdale, G. C. Bazan, *Adv. Mater.* **2011**, *23*, 2367.